ADVANCED MATERIALS
www.advmat.de

Unconventional Band Structure via Combined Molecular Orbital and Lattice Symmetries in a Surface-Confined Metallated Graphdiyne Sheet

Ignacio Piquero-Zulaica, Wenqi Hu, Ari Paavo Seitsonen, Felix Haag, Johannes Küchle, Francesco Allegretti, Yuanhao Lyu, Lan Chen, Kehui Wu, Zakaria M. Abd El-Fattah, Ethem Aktürk, Svetlana Klyatskaya, Mario Ruben, Matthias Muntwiler, Johannes V. Barth,* and Yi-Qi Zhang**

Graphyne (GY) and graphdiyne (GDY)-based monolayers represent the next generation 2D carbon-rich materials with tunable structures and properties surpassing those of graphene. However, the detection of band formation in atomically thin GY/GDY analogues has been challenging, as both long-range order and atomic precision have to be fulfilled in the system. The present work reports direct evidence of band formation in on-surface synthesized metallated Ag-GDY sheets with mesoscopic (≈1 µm) regularity. Employing scanning tunneling and angle-resolved photoemission spectroscopies, energy-dependent transitions of real-space electronic states above the Fermi level and formation of the valence band are respectively observed. Furthermore, density functional theory (DFT) calculations corroborate the observations and reveal that doubly degenerate frontier molecular orbitals on a honeycomb lattice give rise to flat, Dirac and Kagome bands close to the Fermi level. DFT modeling also indicates an intrinsic band gap for the pristine sheet material, which is retained for a bilayer with *h*-BN, whereas adsorption-induced in-gap electronic states evolve at the synthesis platform with Ag-GDY decorating the (111) facet of silver. These results illustrate the tremendous potential for engineering novel band structures via molecular orbital and lattice symmetries in atomically precise 2D carbon materials.

1. Introduction

The synthesis and characterization of π-conjugated 2D polymers with atomic thickness and covalently bonded periodic structures have recently been pushed to the forefront of research in chemistry and physics,[1–4] concomitant with the rapidly advancing exploration of 2D materials.[5–7] Through a suitable choice of molecular building blocks and linking motifs, crystalline 2D organic polymers or hybrid metal-organic sheets can be rationally designed with tailored electronic properties, including π-orbital overlapping, dispersive bands as well as adjustable band gap,[8,9] which are essential for applications in organic electronics.[10,11] In particular, theoretical modeling shows that a proper combination of frontier molecular orbital (MO) and lattice symmetries opens up new avenues toward realizing unconventional

I. Piquero-Zulaica, F. Haag, J. Küchle, F. Allegretti, J. V. Barth, Y.-Q. Zhang
Physics Department E20
Technical University of Munich
D-85748 Garching, Germany
E-mail: ge46biq@mytum.de; jvb@tum.de

W. Hu, Y. Lyu, L. Chen, K. Wu, Y.-Q. Zhang
Institute of Physics
Chinese Academy of Sciences
Beijing 100190, China
E-mail: yiqi.zhang@iphy.ac.cn

A. P. Seitsonen
Département de Chemie
École Normale Supérieure
24 rue Lhomond, Paris F-75005, France

Z. M. A. El-Fattah
Physics Department
Faculty of Science
Al-Azhar University
Nasr City, Cairo E-11884, Egypt

The ORCID identification number(s) for the author(s) of this article can be found under https://doi.org/10.1002/adma.202405178

DOI: 10.1002/adma.202405178

Z. M. A. El-Fattah
Physics Department
Faculty of Science
Galala University
New Galala City, Suez 43511, Egypt

E. Aktürk
Department of Physics
Adnan Menderes University
Aydin 09100, Turkey

S. Klyatskaya, M. Ruben
Institute of Nanotechnology
Karlsruhe Institute of Technology
76344 Eggenstein-Leopoldshafen, Germany

M. Ruben
IPCMS-CNRS
Université de Strasbourg
23 rue de Loess, Strasbourg 67034, France

M. Muntwiler
Paul Scherrer Institute
Forschungsstrasse 111
Villigen PSI 5232, Switzerland

band structures in these materials, such as flat, Dirac and Kagome bands,[12–15] which can be further tailored to give rise to novel topological or many-body states.[13,14,16]

Among various types of π-conjugated 2D polymers, a special class of carbon-based networks distinct from graphene, known as graphyne (GY).[17] and graphdiyne (GDY).[18] is of particular interest.[3,19] The incorporation of acetylenic precursors containing carbon-carbon triple bonds (—C≡C—) enables creating a great variety of GY/GDY-related structures with *sp*- and sp^2-hybridized carbon atoms,[20] offering remarkable tunability in their physical and chemical properties.[19,21] However, synthesizing crystalline GY/GDY sheets as well as their analogues turned out to be particularly challenging,[19] which hampers in-depth electronic structure characterizations. The past fifteen years witnessed the rapid growth in the field of on-surface synthesis in ultra-high vacuum (UHV),[22,23] providing new access to synthesize 2D polymers via the bottom-up approach,[24] and many exemplary carbon-based architectures have been achieved.[25–29] Recently, utilizing a terminal alkyne derivative 1,3,5-tris(4-ethynylphenyl)benzene (Ext-TEB)[30] and a highly chemoselective gas-mediated on-surface reaction protocol, we fabricated a highly regular mesoscale (≈1 µm) organometallic monolayer,[31] formally representing an Ag-metallated graphdiyne (Ag-GDY) analogue. Therefore, it provides an ideal platform to scrutinize the electronic properties of atomically well-defined metallated GDY sheets.

In this work, employing scanning tunneling microscopy and spectroscopy (STM/STS), angle-resolved photoelectron spectroscopy (ARPES) and density functional theory (DFT), we show that the intrinsic electronic structure of Ag-GDY corresponds to a hole-doped semiconductor with an unconventional band structure. Notably, both the conduction band minimum (CBM) and the valence band maximum (VBM) comprise nontrivial flat bands, arising from the combined molecular orbital and lattice symmetries. STS and ARPES measurements respectively detect the onsets of CBM and VBM with an energy separation (ΔE), $\Delta E_{\text{CBM-VBM}}$ ≈2.5 eV. The VBM positioning below the Fermi level reveals the presence of mild adlayer-substrate electronic hybridization, potentially entailing in-gap electronic features. DFT calculations corroborate the experimental results and further reveal that employing an insulating buffer layer may restore the Ag-GDY intrinsic band structure with a flat band residing near the Fermi level, which is important for tuning correlated electronic behavior in such systems.

2. Results and Discussion

2.1. Emerging Novel Band Structure in Freestanding Ag-GDY

The Ag-GDY network (see chemical scheme in right panel of **Figure 1b**) presents unique structural characteristics, featuring a honeycomb lattice occupied by Ext-TEB molecules and a Kagome lattice spanned by alkynyl-Ag atoms (cf. highlighted grids in Figure 1b, left panel). The Ag-GDY network is expected to harbor dispersive bands as Ext-TEB is aromatic[32] and the Ag-intercalated butadiyne bridge (—C≡C—Ag—C≡C—) has covalent character.[33] As a first step, the electronic band structure of the freestanding layer with a rhombic unit cell containing two Ext-TEB molecules and three silver atoms was calculated (cf. Figure 1c and Figure S1, Supporting Information). The CBs of the network start at ≈2.4 eV above the Fermi level (Figure 1c). The first group (CB_1) features two Dirac bands sandwiched between two nearly flat bands, whereas the second group (CB_2) contains only two Dirac bands. The VBs reach 0.03 eV above the Fermi level, comprising two consecutive sets of Kagome bands (cf. VB_1 and VB_2 in Figure 1c). It is unusual that both the lowest CB and the highest VB are flat bands, and these features are reminiscent of the typical band structure predicted from a honeycomb lattice with doubly degenerate on-site orbitals.[12–14]

To further examine the network band structure characteristics, MOs of Ext-TEB were calculated (cf. Figure 1a and Figure S2, Supporting Information). The lowest unoccupied and the highest occupied molecular orbitals (LUMO/HOMO) both display double degeneracy, related to the threefold symmetry of the molecule (Figure 1a). DFT calculations also show that LUMO+1 and HOMO-1 for Ext-TEB are single levels with different ΔE to LUMO and HOMO (Figure 1a), respectively.

The band structure of the Ag-GDY network can be reproduced using a tight-binding model outlined by Ni et al,[13] employing a three-orbital (σ, π_x, π_y) basis on a honeycomb lattice, which results in six bands. When the ΔE between the degenerate (π_x, π_y)-MOs and the single σ-MO is large (ΔE = 0.4 eV; red box in Figure 1a), the former yields four bands corresponding to CB_1 (Figure 1c), while the latter produces two Dirac bands (CB_2). Alternatively, a small ΔE (ΔE = 0.23 eV; blue box in Figure 1a) causes hybridization between σ and (π_x, π_y)-MOs, yielding two sets of Kagome bands,[13] corresponding to the Ag-GDY VB edge (VB_1 and VB_2 in Figure 1c). To further verify the band composition, we examine isosurfaces of orbital density integrated within the selected band groups (Figure 1d), along with the band structure projected onto molecular orbitals (Figure S3, Supporting Information). It is clear that CB_1 exclusively originates from the degenerated LUMOs, while CB_2 is contributed from the single LUMO+1. Notably, VB_1 is contributed by both HOMO and HOMO-1, and so is VB_2. Therefore, the emergence of flat, Dirac as well as Kagome bands close to the Fermi level can be rationalized based on the frontier MO and lattice symmetries of the Ag-GDY network. Another intriguing feature of the band structure is that the Fermi level intersects slightly below the flat top VB, which is attributed to the open shell character of the alkynyl-Ag bridge.[33–35] Accordingly, isolated Ag-GDY sheets show hole-doped semiconductor characteristics with leading flat bands enclosing a gap of E_g ≈2.4 eV.

2.2. Energy-Dependent Evolution of Electronic States

High-quality samples are essential for electronic properties characterization. The overview STM image in **Figure 2a** depicts the regular Ag-GDY network prepared on the Ag(111) single crystal surface, covering an area of ≈500 × 500 nm^2 without apparent defects (cf. also Figure S4, Supporting Information). The long-range order of the atomically thin film is further confirmed by the corresponding exemplary low-energy electron diffraction (LEED) pattern in Figure 2b, which corresponds to a

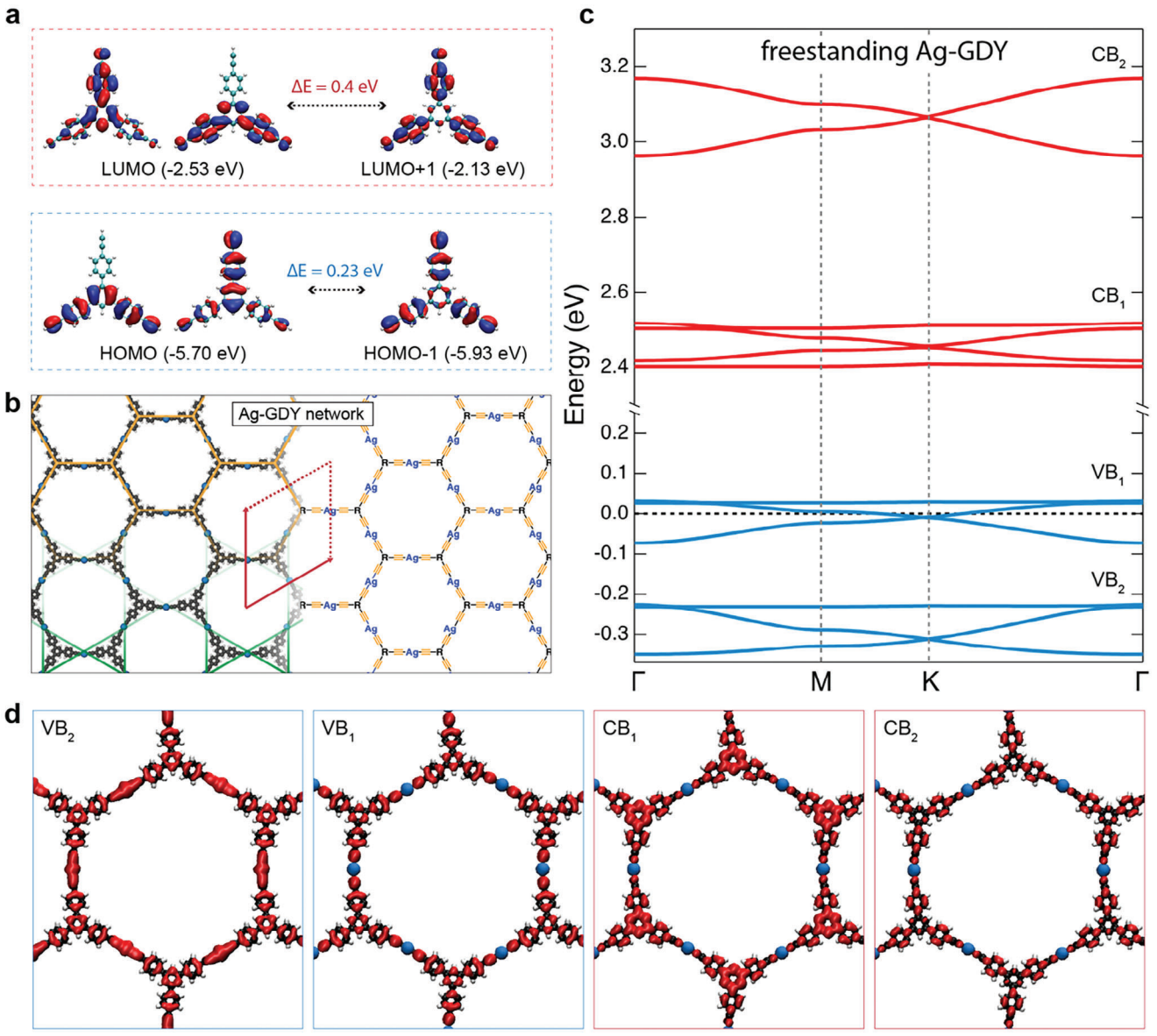

Figure 1. Doubly degenerate precursor LUMO and HOMO account for flat, Dirac and Kagome bands in the Ag-GDY sheet. a) DFT calculated frontier MOs of an isolated Ext-TEB molecule. b) Model and chemical scheme of a freestanding Ag-GDY sheet with rhombic unit cell. Honeycomb and Kagome lattices occupied by molecules and Ag atoms are highlighted, respectively. c) DFT-calculated band structure around the Fermi level and above the band gap of the freestanding network. Red and blue colors are used to distinguish CBs and VBs. d) Integrated network orbital density of the first and second groups of VBs and CBs, respectively.

superposition of reciprocal lattices of domains with three different orientations rotated by 120° relative to each other on Ag(111)[31] (cf. Figure 2c and Figures S5 and S6, Supporting Information). For practical purposes, we also prepared Ag-GDY networks on inexpensive Ag(111)/mica substrates. Notably, the atomically straight steps along high-symmetry directions facilitate continuous network growth across adjacent terraces (see Figure 2d and Figure S7, Supporting Information). This single-layer continuity resembles the main feature of covalently bonded 2D materials (e.g., *h*-BN or graphene sheets).[36,37] On both substrates the network unit cell is rectangular, with parameters a_1 = 63.6 Å, a_2 = 35.0 Å (cf. Figure 2f and Figure S9, Supporting Information).

To elucidate band formation in Ag-GDY, site-dependent differential conductance (dI/dV) spectra as well as bias-dependent dI/dV maps were obtained, focusing on a six-membered ring as the basic constituent of the regular network (cf. **Figure 3c**). Hereby care must be taken to differentiate the appearance of the well-known quantum confinement effects imposed by the nanoporous lattice[38] on the quasi-2D electron gas provided by the Ag(111) surface state (SS) from the electronic properties of the Ag-GDY sheet.

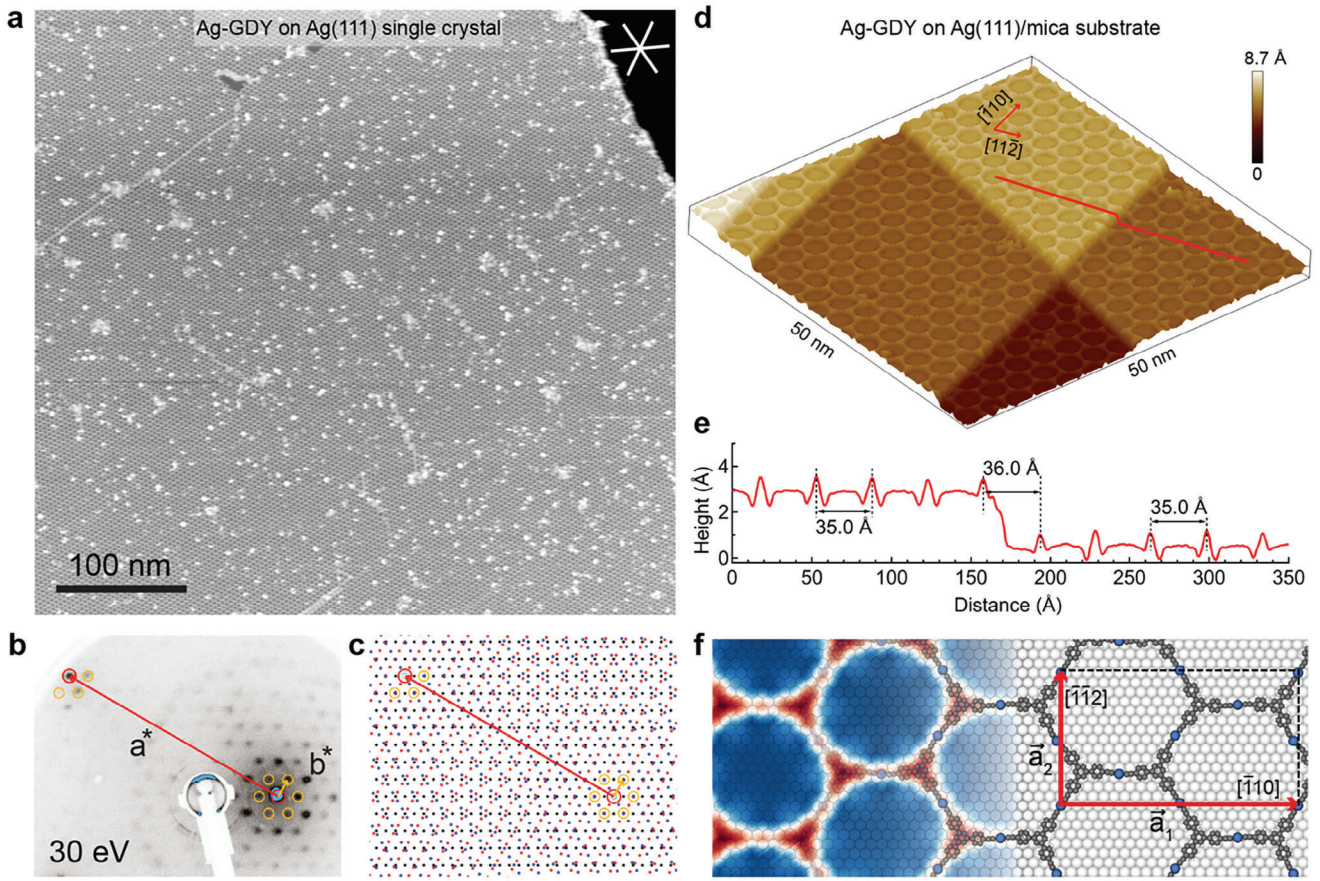

Figure 2. Overview STM images of Ag-GDY network grown on Ag(111) facets. a) STM image of a continuous 500 × 500 nm^2 atomically thin Ag-GDY network grown on an Ag(111) single crystal. I_t = 100 pA, U_b = −1.0 V. b) LEED pattern of Ag-GDY/Ag(111) for T_{sub} = 90 K and $E_{electron}$ = 30 eV. c) Modeling of the LEED pattern. d) 3D rendering of an STM image showing the continuity of the network crossing straight steps on Ag(111)/mica. I_t = 50 pA, U_b = 0.1 V. e) STM contour of line marked in (d). f) Structure model of Ag-GDY network with rectangular unit cell on Ag(111) facet.

Figure 3a depicts point spectra recorded on Ag surface (black and grey curves), Ext-TEB molecules (red) and alkynyl-Ag atoms (blue) in a bias range from −0.2 to 1.2 V. The data taken at the pore center (black curve) displays three main peaks at 81, 328 and 677 mV, corresponding to the first, second and fourth (n = 1, 2, 4) resonances of confined substrate Shockley-SS electrons in the nanocavity[38] (unrelated to the 2D polymer). The solid red curve in Figure 3a is averaged over six molecular sites in the hexagonal unit (red mark in Figure 3c). Genuine band formation is first evidenced by the fact that the dI/dV spectra taken at six molecular sites are nearly identical (cf. dimmed red curves in Figure 3a), whereas this conformity was absent in isolated hexamers or disordered network patches (cf. Figure S10, Supporting Information). The second indication is given by the emergence of a peak with onset at 464 mV, followed by three further peaks when sweeping up to 1000 mV (respectively indicated by a red arrow and black bars in Figure 3a). These energy positions correspond neither to confined SS electrons nor to single Ext-TEB units, as both exhibit featureless local density of states (LDOS) in this bias range.[32] The spectrum taken on the alkynyl-Ag atoms shows merely a steadily increasing intensity (blue curve in Figure 3a). Figure 3b displays dI/dV spectra taken at the same positions with a larger bias range. Again, their shapes do not vary at equivalent sites. The averaged spectrum on Ext-TEB units peaks at ≈2200 mV (cf. red star in Figure 3b), whereas for the Ag-bridge sites a single broad peak dominates at ≈2050 mV, markedly downshifted when compared to the characteristic signature at 2.9 V of an individual Ag adatom on Ag(111).[39]

Real-space electronic states associated with SS confinement and intrinsic Ag-GDY band formation appear clearly in bias-dependent dI/dV maps (Figure 3d) with energy positions indicated in Figure 3a,b. At low biases, the imaged LDOS within the nanopore reflects typical intensity patterns of confined SS electrons (n = 1 and 2; Figure 3d-1,2). For a bias V_B of 464 mV (Figure 3d-3), localized LDOS intensity clearly appears on the triangular-shaped Ext-TEB backbone, whence it is associated with the CBM (cf. Figure 3a). With further increasing bias the LDOS extends to the Ag-bridge sites, until a uniform honeycomb grid evolves at 677 mV, indicating delocalized electronic character (Figure 3d-4,5 and Figure S11, Supporting Information). From 756 to 955 mV, the LDOS concentrates on the alkynyl-Ag atoms (Figure 3d-6,7). Most intriguing is the bias range from 1053 to 1355 mV, where the electron density at the molecular edge becomes prominent and merges via the alkynyl-Ag sites to form a Kagome grid at 1355 mV (Figure 3d-8 to 10 and Figure S12, Supporting Information). Examining the even higher bias range

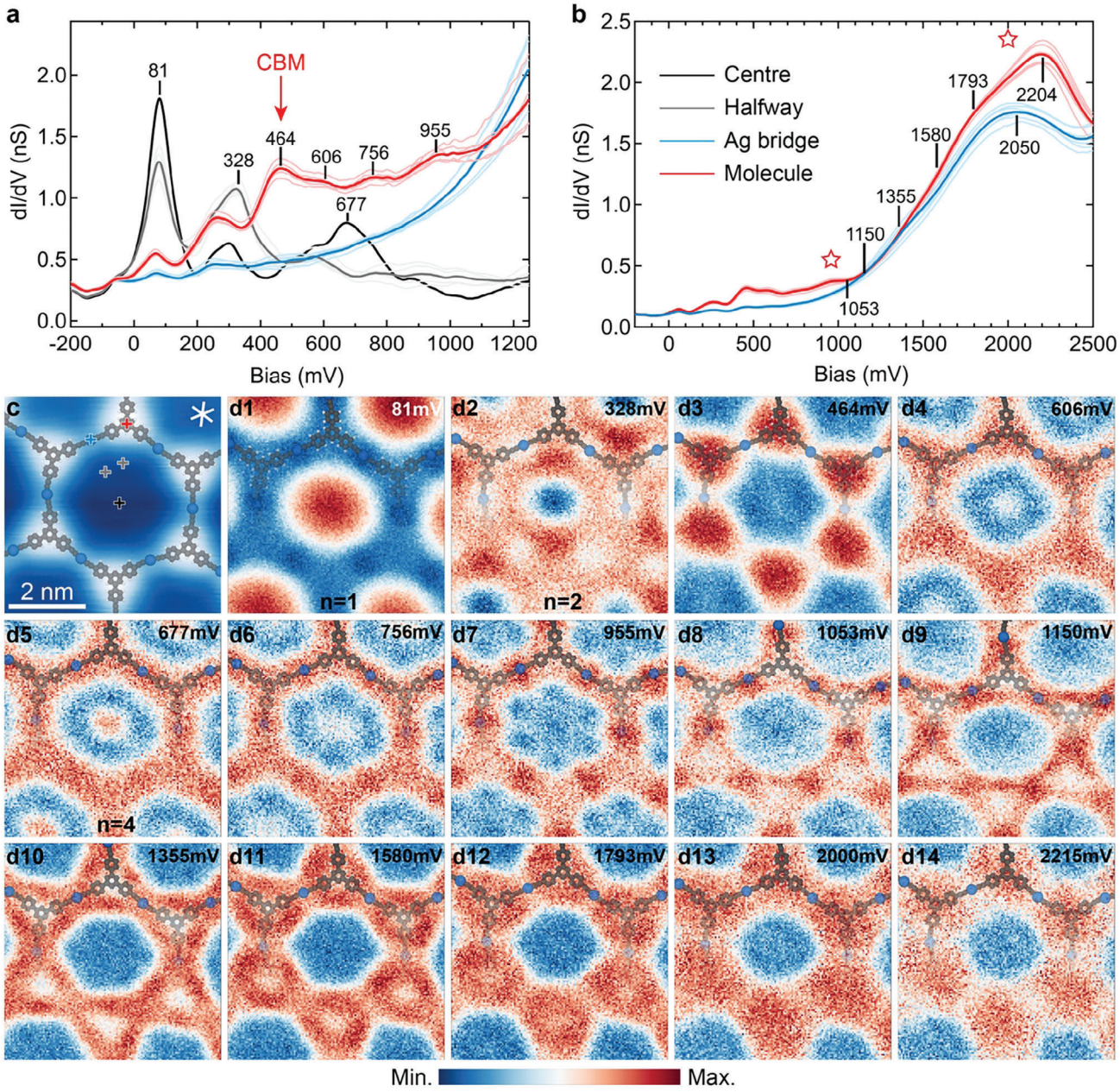

Figure 3. STS characterization of the elementary constituents in a Ag-GDY/Ag(111) sheet. a-b) Site-specific d*I*/d*V* spectra taken in the bias range from −0.2 to 1.2 V and extended bias range from −0.3 to 2.5 V, respectively. The single peak at ≈1 V and the double-peak feature at ≈2 V are highlighted by stars, respectively. Set point: I_t = 50 pA, U_b = −0.2 V and −0.3 V, U_m = 20 mV. c) Corresponding STS survey area in the network, superimposed with a DFT model with rectangular unit cell. I_t = 50 pA, U_b = 0.96 V. d) Bias-dependent d*I*/d*V* mapping of the regular six-membered ring shown in (c). Set point: I_t = 50 pA, U_m = 20 mV.

from 1.5 to 2.2 V, the electronic Kagome grid gradually becomes filled until a nodal plane develops at the Ag-bridge (Figure 3d-11 to 14).

The bias-dependent transitions of periodic electronic states on the molecular lattice, which evolve from localized to itinerant characteristics and further to the electronic Kagome grid, clearly indicate band structure formation in the Ag-GDY sheet. To investigate the VBs (Figure 1c), STS were also measured in the bias range below the Fermi level. However, no significant features were observed (see Figure S13, Supporting Information), similarly to observations in other reported covalent structures adsorbed on metal substrates.[33,40]

2.3. ARPES Observation of Valence-Band Formation

To probe the electronic properties of Ag-GDY in the occupied states regime, complementary ARPES measurements were

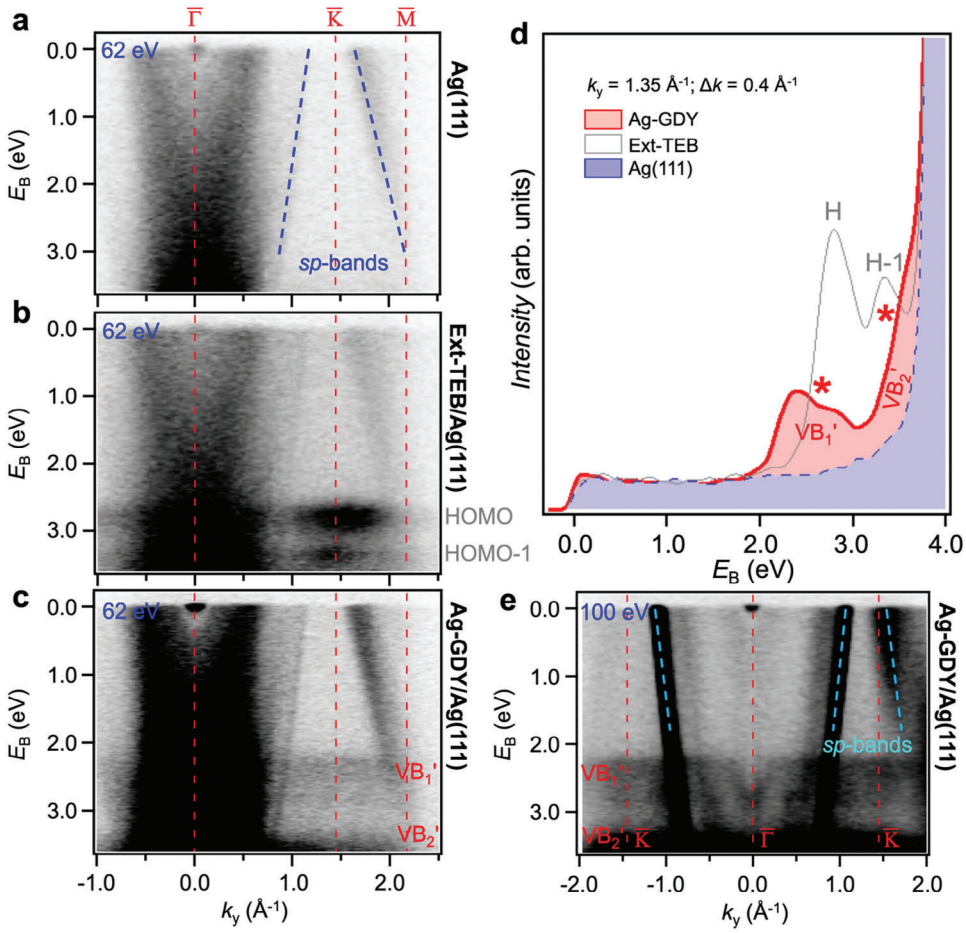

Figure 4. Evolution of ARPES band structure upon Ag-GDY sheet formation. a–c), Band structure (E_B versus k_y) of pristine Ag(111), Ext-TEB organic multilayer and Ag-GDY network measured along the [1$\bar{1}$0] substrate direction (i.e., along $\overline{\Gamma K}$) with a photon energy of 62 eV. d) EDCs extracted at k_y = 1.35 Å^{-1} evidence discrete occupied frontier orbitals for pure Ext-TEB molecules and their transformation to a valence band (VB_1' with a ≈0.8 eV bandwidth; marked with an asterisk) upon Ag-GDY network formation. The additional onset close to the Ag *d*-bands corresponds to the VB_2' (indicated by an asterisk). e) Same band structure as in (c) measured with 100 eV photon energy: While Ag-*sp* bands shift with photon energy, the Ag-GDY bands remain unchanged in accordance with their 2D nature. ARPES experimental datasets in (a) and (b) were obtained at RT, (c) and (e) at T ≈ 60 K (cf. Figure S21, Supporting Information).

carried out for networks grown on Ag(111), exhibiting a sharp LEED pattern (cf. Figure 2b and Figure S14, Supporting Information). As a reference, the band structure $E(k_y)$ of a clean substrate measured along the $\overline{\Gamma K}$ direction of the Ag(111) surface Brillouin zone (BZ) with a photon energy of 62 eV is depicted in **Figure** 4a. The well-known Ag SS surrounded by the projected bulk bands as well as the highly-dispersive *sp*-bands prevail. Since the onset energy of silver *d*-bands is 3.5 eV below the Fermi level (cf. Figure S15, Supporting Information), there is a wide energy window available for exploring the Ag-GDY bands. Next, the occupied frontier orbitals of the intact Ext-TEB molecules were examined using an organic multilayer sample, whereby the nondispersive HOMO and HOMO-1 levels at E_b ≈ 2.8 and 3.2 eV can be clearly discerned with maximal intensity at ≈1.5 Å^{-1}, indicating the absence of delocalized states for the supramolecular assembly (Figure 4b and Figure S16, Supporting Information).[41,42]

In Figure 4c, the band structure for the Ag-GDY fully covering the surface is shown. The previously distinct MOs of individual Ext-TEB (Figure 4b) transform into less prominent intensity features smeared out along the $\overline{\Gamma K}$ direction of the Ag(111) surface BZ in an energy window between E_b ≈ 2 and 3 eV (cf. also Figures S17 and S18c, Supporting Information). The VB formation can be clearly seen in Figure 4d by comparing the energy distribution curves (EDCs) of unreacted Ext-TEB molecules and Ag-GDY extracted in the vicinity of k_y = 1.35 Å^{-1} in Figure 4b,c. The HOMO (H) and HOMO-1 (H-1) peaks (grey curve in Figure 4d) are well separated above the onset of the *d*-bands (purple area at E_b > 3.8 eV), in agreement with the DFT calculation (Figure 1a). In contrast, for the adsorbed Ag-GDY sheet, a wider double-peak feature (marked by an asterisk in Figure 4d) with an onset shifted closer to the Fermi level at E_b ≈ 2.0 eV appears, followed by a much broader increase merged into the silver *d*-bands (E_b ≈ 3.8 eV). The first set of VBs (denoted by VB_1') has a relatively

wide bandwidth of ≈0.8 eV with clear intensity variations, indicating a fine structure due to multiple band contributions (cf. also Figure S18c, Supporting Information). The higher intensity appearing at increased binding energies is attributed to the next set of bands denoted by VB'_2 (cf. the asterisk in Figure 4d). Obviously, the VBM of the adsorbed system shifts below the Fermi level compared to the freestanding layer (Figure 1c), for reasons to be clarified below. Moreover, ARPES data acquired at a photon energy of 100 eV are presented in Figure 4e. The projection of the bulk bands around the $\bar{\Gamma}$ point is strongly attenuated, leading to a better recognition of the VBs. It is evident that VB'_1 and VB'_2 do not change their position with photon energy, whereas the intensity and the $E(k)$ distribution of the highly dispersive *sp*-bands from Ag(111) are altered (cf. also Figure S20, Supporting Information),[43] which supports the conclusion that these VBs originate from the Ag-GDY sheet.[44]

2.4. DFT Modeling of Adsorbed Ag-GDY Network

Experimentally detected CBM and VBM originating from the adsorbed Ag-GDY single sheet allows us to define for the adlayer an energy interval $\Delta E_{\text{CBM-VBM}}$ ≈2.5 eV that is reminiscent of a band gap. However, similar with related systems, the contact and interaction with the metal substrate can entail the development of interfacial electronic states accounting for appreciable density of states.[37,45–47] To develop a better understanding of the experimental results, we carried out systematic DFT calculations of Ag-GDY sheet on a thick Ag(111) slab (cf. Experimental Section). **Figure 5a** displays the projected density of states (PDOS) for each component in the system. In the unoccupied regime, the energy positions of CBM, the single peak at 1 eV, and the double-peak feature at 2 eV in the carbon PDOS agree well with the STS data (highlighted by an arrow and two stars in Figures 3a,b and 5a). In the occupied regime, the VBM sets in at −1.2 eV, followed by two main peaks at −1.7 and −2.7 eV, which can be well correlated with the VB'_1 and VB'_2 in the ARPES data (highlighted by two asterisks in Figures 4d and 5a). The carbon PDOS intensity greatly attenuates in an energy interval ≈1.7 eV between CBM and VBM (grey area in Figure 5a). When comparing PDOS features and differences between Ag-GDY/Ag(111) and freestanding Ag-GDY (Figure S29, Supporting Information), the grey area in Figure 5a can be loosely associated with the gap region of the freestanding layer. However, PDOS builds up within the gap due to a mild hybridization between the alkynyl-Ag-alkynyl organometallic linkage and the silver substrate (cf. also Figures S23 and 24, Supporting Information). Similar effects have been reported for the boron-doped graphene nanoribbons adsorbed on Au(111),[45] or *h*-BN layers synthesized and carefully examined on metal substrates.[37,46,47] Importantly, the pertaining newly formed states exhibit significantly lower intensity as compared to that outside the gap regime and proved thus unresolvable in the photoemission signature (Figure S19, Supporting Information). The variation between experimental and DFT-determined $\Delta E_{\text{CBM-VBM}}$ values can be attributed to the typical underestimation of gap sizes in the DFT calculations.[48,49]

Moreover, Figure 5b displays a series of simulated dI/dV maps, revealing a good match between experimental and simulated images in the appropriate energy ranges. First, the confined Ag SS resonances (n = 1,2) in the nanopore are nicely reproduced due to the employed thick Ag slab (Figure 5b-1,2; cf. also Figure S22, Supporting Information). Second, the bias-dependent evolution of LDOS patterns of the network is captured: starting from localized density on the Ext-TEB core (Figure 5b-3) to displaying a uniform honeycomb electronic pathway (Figure 5b-4), followed by the merging of Ag-bridge (Figure 5b-5) and molecular edge state (Figure 5b-6) into a real-space electronic Kagome grid (Figure 5b-7). Overall, the DFT calculations for the Ag-GDY/Ag(111) system can be nicely reconciled with the experimental observations.

Compared to the freestanding network, the VBs of the adsorbed Ag-GDY on the silver surface notably shift below the Fermi level, indicating that the open shell of the unit cell is filled. An estimate obtained with the Bader charge analysis reveals a total charge transfer of ≈3 electrons from the substrate as well as the bridging silver adatom to compensate six alkynyl radicals in the unit cell. Moreover, the absence of well-defined Kagome-type $E(k)$ relations in the ARPES data can be ascribed to a mild electronic hybridization between the adlayer and the silver surface (cf. Figures S23–S25 and S29, Supporting Information) as well as to a small BZ of the network (Figure S17, Supporting Information). Nevertheless, at CBM (V_B = 464 mV) the LDOS intensity localized on the molecules, as observed in both the experimental and simulated dI/dV maps (Figures 3d-3 and 5b-3), is consistent with the nontrivial-flat-band character, namely, quenched electron kinetic energy due to destructive interference of Bloch waves.[14]

Finally, to assess whether the intrinsic Ag-GDY electronic bands would persist on an insulator, a sheet supported on a *h*-BN monolayer[50] was modeled (**Figure 6a**). Importantly, the leading VBs remain identical as those of the freestanding layer, while CB_1 and CB_2 slightly shift down toward the Fermi level (Figure 6c), resulting in a contourless band gap region without interference of in-gap states (cf. Figures S26–S29, Supporting Information). Remarkably, a finite gap (≈37 meV) opens at the Γ point, which gives rise to an isolated flat band at the bottom of CB_1 (cf. red solid lines in Figure 6c). Also, gap-openings at Dirac points are observed for both CB_1 (≈30 meV) and CB_2 (≈37 meV). Note that the phenyl rings of individual Ext-TEB molecules in the unit cell locate on top of either nitrogen or boron atoms (Figure 6a). Therefore, the geometrical symmetry breaking induced by the bilayer formation presents as an effective mechanism for opening band gaps.[14,16]

3. Conclusion

The achievement of high-quality crystalline Ag-GDY sheets permitted an in-depth electronic structure characterization at both the atomic and mesoscopic scales. Band formation with a semiconducting gap prevails for this π-conjugated GDY analogue as pristine sheet material and in conjunction with *h*-BN providing a bilayer. Moreover, we reveal that Ag-GDY hosts unconventional flat, Dirac and Kagome bands at both conduction and valence band edges, which originate from combined MO and lattice symmetries. On the Ag(111) synthesis platform, mild hybridization between the Ag-GDY sheet and metal surface interferes, entailing in-gap states, which effect can be attenuated via electronic decoupling using an insulating spacer layer. Based on our results,

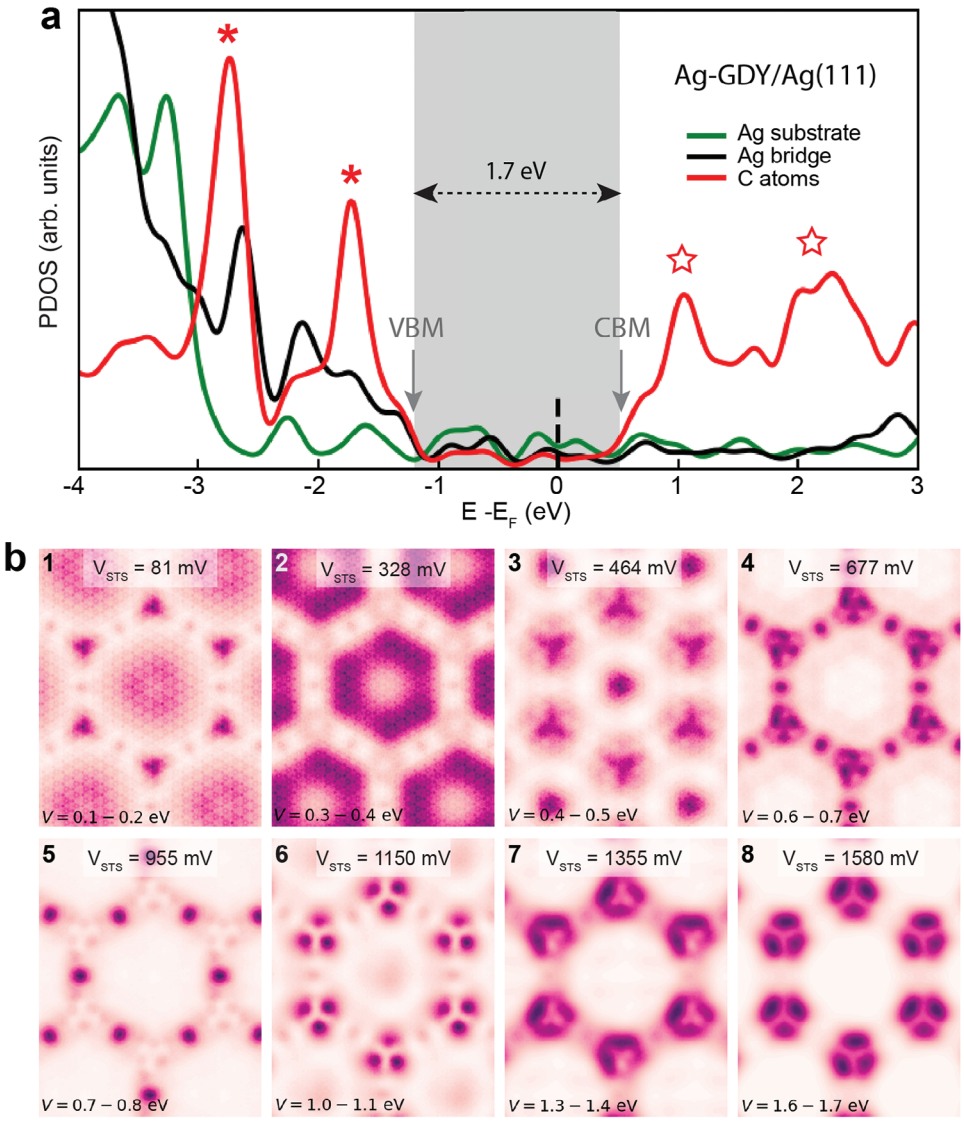

Figure 5. DFT modelization of Ag-GDY/Ag(111) electronic features. a) Projected DOS of the Ag-GDY network adsorbed on four-layer Ag(111) slab. Contributions from carbon, alkynyl-Ag atoms and substrate are distinguished by different colors. The main peaks in the carbon PDOS are highlighted by asterisks and stars in accordance with those in Figures 3b and 4d. The plotted PDOS intensity for each constituent is arbitrary. b) Simulated *dI/dV* maps with characteristic LDOS patterns corresponding to the experimental bias values, indicated on the top of each panel.

replacing the molecular units and different metallation schemes can be envisioned. Therefore, the proper combination of MO characteristics and lattice symmetry can give access to bespoke novel electronic structures, unfolding exciting opportunities for tailored 2D material developments amenable to device-integrated applications.

4. Experimental Section

Sample Preparation: The Ag-GDY networks were prepared under UHV conditions. Ag(111) single crystals and Ag(111)/mica substrates were used for sample growth. Ext-TEB precursors were evaporated from Al_2O_3 or quartz crucibles onto clean Ag(111) surfaces held at ≈200– 300 K, followed by an alkyne deprotonation procedure via introducing O_2 gas (≈ 1000 L) into the preparation chamber by backfilling via a leak valve. The sample was mildly annealed (T_{ann} ≈ 400 K) to facilitate the organometallic network formation.

STM/STS Characterization: A commercial Joule-Thomson STM (JT-STM, SPECS) and a homemade LT-STM were used for data acquisition. Data was recorded at an equilibrium temperature of ≈5 K. Point STS spectroscopy were measured via a lock-in amplifier with a bias modulation of 20 mV at 676 Hz. d*I*/d*V* maps were recorded at fixed bias voltage in a grid with 128 × 128 pixels, and the feedback was switched off during d*I*/d*V* signal acquisition at each pixel. All the d*I*/d*V* maps were normalized via applying (d*I*/d*V*)/(*I*/*V*), which leads to a better signal to noise ratio without altering the LDOS features.

ARPES Measurements: The ARPES experiments presented in this work were carried out at the Photo-Emission and Atomic Resolution Laboratory (PEARL) of the Swiss Light Source (SLS). The PEARL beamline delivers tunable soft X-ray photons in the energy range from 60 to 2000 eV with a resolving power up to E/ΔE = 7000. The present work used photon energies of 62 and 100 eV to maximize the surface sensitivity.

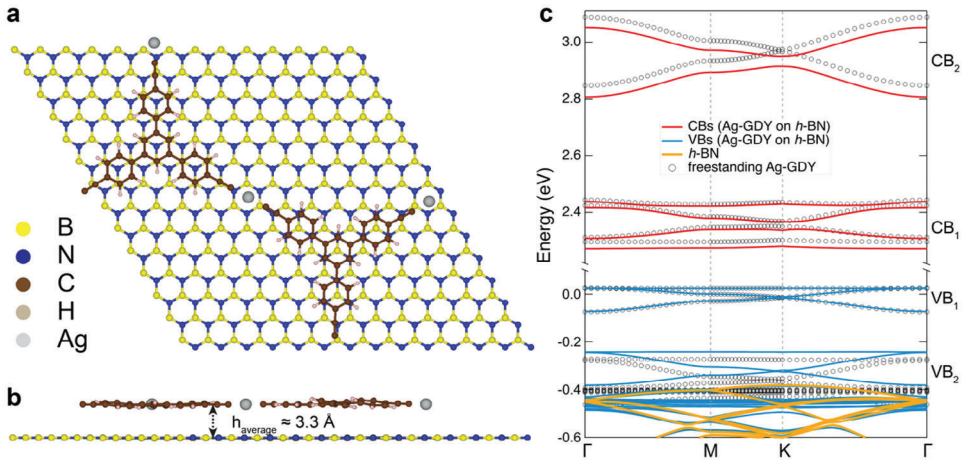

Figure 6. DFT calculated band structure of Ag-GDY sheet on *h*-BN. a-b), Top and side views of the large Ag-GDY/*h*-BN unit cell with averaged adsorption height indicated. c) Band structure of Ag-GDY/*h*-BN (red and blue solid lines) compared with freestanding Ag-GDY (black circles) with same geometry adopted from the combined system shown in (a). *h*-BN bands, which are back-folded due to the employed (14 × 14) supercell (cf. Method), are highlighted in orange. The *k*-path corresponds to that in the hexagonal BZ of the Ag-GDY network.

Samples were mounted on a high-precision manipulator with three translation and three rotation axes. Photoelectrons were detected by a Scienta EW4000 wide acceptance angle analyzer with a 2D multi-channel plate detector where one axis corresponds to the kinetic energy of the electron and the other axis to the emission angle. The entrance lens stack of the analyzer was at a fixed angle of 60° with respect to the incoming synchrotron light. The incoming photon beam, the polarization vector of photons, and the axis of the analyzer lens were oriented horizontally, while the entrance slit of the electron analyzer was oriented vertically. Samples were measured either at RT or at 60 K. A LEED setup mounted on the experimental chamber was also used to assess the surface order as well as the sample orientation.

DFT Calculations: Total energy calculations were performed using DFT within the Kohn–Sham formalism[51] using the Quantum ESPRESSO code.[52] This work used the rB86-vdW-DF2 approximation in the term of the exchange-correlation functional,[53] and only the $\bar{\Gamma}$ point in the integration over the first BZ due to the very large super-cell. Projector augmented wave[54] data sets were applied to remove the core electron from the explicit calculation. STM simulations were performed with the Tersoff–Hamann model,[55] approximating an *s*-wave tip.

This work performed the calculations of the supported network in a hexagonal super-cell, unlike in Ref. [31] where a rectangular, elongated cell was used. In order to reduce the stress in the overlayer the lateral lattice constant of the substrate was slightly adjusted to 4.188 Å so that the average distance between the bridging Ag ad-atoms was the same as in the large system. During the relaxation and analysis of the electronic structure four layers of the substrate and a passivating layer of hydrogen were used at the bottom of the slab, and each layer of the substrate and the passivating layer consisted of 147 atoms, yielding a lateral network lattice constant of 35.904 Å. In the calculations of the band structure, this work could afford to include only two top- most layers of substrate layers. The cut-off energies for wave functions and the electron density were 35 and 500 Ry, respectively.

In the calculation of the Ag-GDY network on the *h*-BN, a (14 × 14) super cell of latter was included with the same Ag-GDY network parameters as those for the silver substrate, whereby all the atoms were allowed to relax in any direction.

Supporting Information

Supporting Information is available from the Wiley Online Library or from the author.

Acknowledgements

I.P.Z., W.H., and A.P.S. contributed equally to this work. This work is financially supported by the National Natural Science Foundation of China (12174431 and 1192780039) and the National Key R&D Program of China (2021YFA1400502, 2021YFA1202902, 2023YFA1407000). J.V.B. acknowledges support from ERC (Advanced Grant MolArt 247299), the Munich Quantum Center, and the DFG Excellence Cluster e-conversion. F.H., J.K., J.V.B. and F.A. acknowledge funding by the German Research Foundation (DFG) through the TUM International Graduate School of Science and Engineering (IGSSE, GSC81). E.A. acknowledges the Alexander von Humboldt Foundation for a Research Fellowship for Experienced Researchers. The calculations were partially performed at the Leibniz Supercomputing Centre. S.K and M.R. acknowledge funding by the DFG through the priority programs 1928 COORNETs and European Union's Framework Programme for Research and Innovation, Horizon 2020, under the Marie Sklodowska-Curie Grant Agreement No. 847471 (QUSTEC). The authors gratefully acknowledge the Paul Scherrer Institut (Villigen, Switzerland) for the provision of synchrotron radiation beamtime at PEARL beamline of the SLS. The authors also thank Willi Auwärter for helpful discussions.

Conflict of Interest

The authors declare no conflict of interest.

Data Availability Statement

The data that support the findings of this study are available from the corresponding author upon reasonable request.

Keywords

angle-resolved photoelectron spectroscopy, band structure, on-surface synthesis, scanning tunneling spectroscopy, π-conjugated polymer

Received: April 11, 2024
Published online: May 29, 2024

[1] J. Sakamoto, J. van Heijst, O. Lukin, A. D. Schlüter, *Angew. Chem., Int. Ed.* **2009**, *48*, 1030.
[2] J. W. Colson, W. R. Dichtel, *Nat. Chem.* **2013**, *5*, 453.
[3] A. Hirsch, *Nat. Mater.* **2010**, *9*, 868.
[4] C. Backes, A. M. Abdelkader, C. Alonso, A. Andrieux-Ledier, R. Arenal, J. Azpeitia, N. Balakrishnan, L. Banszerus, J. Barjon, R. Bartali, S. Bellani, C. Berger, R. Berger, M. M. B. Ortega, C. Bernard, P. H. Beton, A. Beyer, A. Bianco, P. Bøggild, F. Bonaccorso, G. B. Barin, C. Botas, R. A. Bueno, D. Carriazo, A. Castellanos-Gomez, M. Christian, A. Ciesielski, T. Ciuk, M. T. Cole, J. Coleman, et al., *2D Materials* **2020**, *7*, 022001.
[5] R. Mas-Ballesté, C. Gómez-Navarro, J. Gómez-Herrero, F. Zamora, *Nanoscale* **2011**, *3*, 20.
[6] S. Z. Butler, S. M. Hollen, L. Cao, Y. Cui, J. A. Gupta, H. R. Gutiérrez, T. F. Heinz, S. S. Hong, J. Huang, A. F. Ismach, E. Johnston-Halperin, M. Kuno, V. V. Plashnitsa, R. D. Robinson, R. S. Ruoff, S. Salahuddin, J. Shan, L. Shi, M. G. Spencer, M. Terrones, W. Windl, J. E. Goldberger, *ACS Nano* **2013**, *7*, 2898.
[7] K. S. Novoselov, A. Mishchenko, A. Carvalho, A. H. C. Neto, *Science* **2016**, *353*, aac9439.
[8] R. Gutzler, *Phys. Chem. Chem. Phys.* **2016**, *18*, 29092.
[9] R. Gutzler, D. F. Perepichka, *J. Am. Chem. Soc.* **2013**, *135*, 16585.
[10] M. Fahlman, S. Fabiano, V. Gueskine, D. Simon, M. Berggren, X. Crispin, *Nat. Rev. Mater.* **2019**, *4*, 627.
[11] Y. Liu, V. V. Duzhko, Z. A. Page, T. Emrick, T. P. Russell, *Acc. Chem. Res.* **2016**, *49*, 2478.
[12] C. Wu, D. Bergman, L. Balents, S. Das Sarma, *Phys. Rev. Lett.* **2007**, *99*, 070401.
[13] X. Ni, H. Li, F. Liu, J.-L. Brédas, *Mater. Horiz.* **2022**, *9*, 88.
[14] W. Jiang, X. Ni, F. Liu, *Acc. Chem. Res.* **2021**, *54*, 416.
[15] S. Thomas, H. Li, C. Zhong, M. Matsumoto, W. R. Dichtel, J.-L. Bredas, *Chem. Mater.* **2019**, *31*, 3051.
[16] M. A. Springer, T.-J. Liu, A. Kuc, T. Heine, *Chem. Soc. Rev.* **2007**, *49*,2020.
[17] R. H. Baughman, H. Eckhardt, M. Kertesz, *J. Chem. Phys.* **1987**, *87*, 6687.
[18] M. M. Haley, S. C. Brand, J. J. Pak, *Angew. Chem., Int. Ed.* **1997**, *36*, 836.
[19] C. S. Huang, Y. J. Li, N. Wang, Y. R. Xue, Z. C. Zuo, H. B. Liu, Y. L. Li, *Chem. Rev.* **2018**, *118*, 7744.
[20] F. Diederich, M. Kivala, *Adv. Mater.* **2010**, *22*, 803.
[21] D. Malko, C. Neiss, F. Vines, A. Görling, *Phys. Rev. Lett.* **2012**, *108*, 086804.
[22] S. Clair, D. G. de Oteyza, *Chem. Rev.* **2019**, *119*, 4717.
[23] L. Grill, S. Hecht, *Nat. Chem.* **2020**, *12*, 115.
[24] J. V. Barth, G. Costantini, K. Kern, *Nature* **2005**, *437*, 671.
[25] F. Klappenberger, Y.-Q. Zhang, J. Björk, S. Klyatskaya, M. Ruben, J. V. Barth, *Acc. Chem. Res.* **2015**, *48*, 2140.
[26] C. Moreno, M. Vilas-Varela, B. Kretz, A. Garcia-Lekue, M. V. Costache, M. Paradinas, M. Panighel, G. Ceballos, S. O. Valenzuela, D. Pena, A. Mugarza, *Science* **2018**, *360*, 199.
[27] G. Galeotti, F. De Marchi, E. Hamzehpoor, O. MacLean, M. Rajeswara Rao, Y. Chen, L. V. Besteiro, D. Dettmann, L. Ferrari, F. Frezza, P. M. Sheverdyaeva, R. Liu, A. K. Kundu, P. Moras, M. Ebrahimi, M. C. Gallagher, F. Rosei, D. F. Perepichka, G. Contini, *Nat. Mater.* **2020**, *19*, 874.
[28] Q. Fan, L. Yan, M. W. Tripp, O. Krejčí, S. Dimosthenous, S. R. Kachel, M. Chen, A. S. Foster, U. Koert, P. Liljeroth, J. M. Gottfried, *Science* **2021**, *372*, 852.
[29] L. Grossmann, B. T. King, S. Reichlmaier, N. Hartmann, J. Rosen, W. M. Heckl, J. Björk, M. Lackinger, *Nat. Chem.* **2021**, *13*, 730.
[30] Y.-Q. Zhang, N. Kepcija, M. Kleinschrodt, K. Diller, S. Fischer, A. C. Papageorgiou, F. Allegretti, J. Bjork, S. Klyatskaya, F. Klappenberger, M. Ruben, J. V. Barth, *Nat. Commun.* **2012**, *3*, 1286.
[31] Y.-Q. Zhang, T. Paintner, R. Hellwig, F. Haag, F. Allegretti, P. Feulner, S. Klyatskaya, M. Ruben, A. P. Seitsonen, J. V. Barth, F. Klappenberger, *J. Am. Chem. Soc.* **2019**, *141*, 5087.
[32] Y.-Q. Zhang, J. Björk, J. V. Barth, F. Klappenberger, *Nano Lett.* **2016**, *16*, 4274.
[33] Z. Yang, J. Gebhardt, T. A. Schaub, T. Sander, J. Schönamsgruber, H. Soni, A. Görling, M. Kivala, S. Maier, *Nanoscale* **2018**, *10*, 3769.
[34] Y. Chen, Q. Sun, *J. Chem. Phys.* **2017**, 147.
[35] Z. Yang, T. Sander, J. Gebhardt, T. A. Schaub, J. Schonamsgruber, H. R. Soni, A. Gorling, M. Kivala, S. Maier, *ACS Nano* **2020**, *14*, 16887.
[36] H. Tetlow, J. Posthuma de Boer, I. J. Ford, D. D. Vvedensky, J. Coraux, L. Kantorovich, *Phys. Rep.* **2014**, *542*, 195.
[37] W. Auwärter, *Surf. Sci. Rep.* **2019**, *74*, 1.
[38] I. Piquero-Zulaica, J. Lobo-Checa, Z. M. A. El-Fattah, J. E. Ortega, F. Klappenberger, W. Auwärter, J. V. Barth, *Rev. Mod. Phys.* **2022**, *94*, 045008.
[39] A. Sperl, J. Kröger, R. Berndt, A. Franke, E. Pehlke, *New J Phys* **2009**, *11*, 063020.
[40] D. J. Rizzo, Q. Q. Dai, C. Bronner, G. Veber, B. J. Smith, M. Matsumoto, S. Thomas, G. D. Nguyen, P. R. Forrester, W. Zhao, J. H. Jorgensen, W. R. Dichtel, F. R. Fischer, H. Li, J. L. Bredas, M. F. Crommie, *Nano Lett.* **2020**, *20*, 963.
[41] H. Offenbacher, D. Lüftner, T. Ules, E. M. Reinisch, G. Koller, P. Puschnig, M. G. Ramsey, *J. Electron Spectrosc. Relat. Phenom.* **2015**, *204*, 92.
[42] G. Vasseur, M. Abadia, L. A. Miccio, J. Brede, A. Garcia-Lekue, D. G. de Oteyza, C. Rogero, J. Lobo-Checa, J. E. Ortega, *J. Am. Chem. Soc.* **2016**, *138*, 5685.
[43] C. Udhardt, F. Otto, T. Huempfner, B. Schröter, R. Forker, T. Fritz, *J. Electron Spectrosc. Relat. Phenom.* **2018**, *227*, 40.
[44] B. Feng, R.-W. Zhang, Y. Feng, B. Fu, S. Wu, K. Miyamoto, S. He, L. Chen, K. Wu, K. Shimada, T. Okuda, Y. Yao, *Phys. Rev. Lett.* **2019**, *123*, 116401.
[45] E. Carbonell-Sanromà, A. Garcia-Lekue, M. Corso, G. Vasseur, P. Brandimarte, J. Lobo-Checa, D. G. de Oteyza, J. Li, S. Kawai, S. Saito, S. Yamaguchi, J. E. Ortega, D. Sánchez-Portal, J. I. Pascual, *J. Phys. Chem. C* **2018**, *122*, 2512.
[46] A. B. Preobrajenski, S. A. Krasnikov, A. S. Vinogradov, M. L. Ng, T. Käämbre, A. A. Cafolla, N. Mårtensson, *Phys. Rev. B* **2008**, *77*, 085421.
[47] M. Thaler, D. Steiner, A. Menzel, F. Mittendorfer, E. Bertel, *Phys. Rev. Res.* **2020**, *2*, 043156.
[48] J. P. Perdew, W. Yang, K. Burke, Z. Yang, E. K. U. Gross, M. Scheffler, G. E. Scuseria, T. M. Henderson, I. Y. Zhang, A. Ruzsinszky, H. Peng, J. Sun, E. Trushin, A. Görling, *Proc. Natl. Acad. Sci. U.S.A.* **2017**, *114*, 2801.
[49] K. Sohlberg, M. E. Foster, *RSC Adv.* **2020**, *10*, 36887.
[50] M. Topsakal, E. Aktürk, S. Ciraci, *Phys. Rev. B* **2009**, *79*, 115442.
[51] P. Hohenberg, W. Kohn, *Phys. Rev.* **1964**, *136*, B864.
[52] G. Paolo, B. Stefano, B. Nicola, C. Matteo, C. Roberto, C. Carlo, C. Davide, L. C. Guido, C. Matteo, D. Ismaila, C. Andrea Dal, G. de Stefano, F. Stefano, F. Guido, G. Ralph, G. Uwe, G. Christos, K. Anton, L. Michele, M.-S. Layla, M. Nicola, M. Francesco, M. Riccardo, P. Stefano, P. Alfredo, P. Lorenzo, S. Carlo, S. Sandro, S. Gabriele, P. S. Ari, et al., *J. Phys.: Condens. Matter* **2009**, *21*, 395502.
[53] I. Hamada, *Phys. Rev. B* **2014**, *89*.
[54] P. E. Blöchl, *Phys. Rev. B* **1994**, *50*, 17953.
[55] J. Tersoff, D. R. Hamann, *Phys. Rev. B* **1985**, *31*, 805.